Commun. Comput. Phys.
doi: 10.4208/cicp.071210.040511a

Vol. **11**, No. 3, pp. 831-862
March 2012

A Variational Model for Two-Phase Immiscible Electroosmotic Flow at Solid Surfaces

Sihong Shao[1] and Tiezheng Qian[2,*]

[1] *Joint KAUST-HKUST Micro/Nanofluidics Laboratory, Hong Kong University of Science and Technology, Clear Water Bay, Hong Kong; LMAM and School of Mathematical Sciences, Peking University, Beijing 100871, China.*
[2] *Department of Mathematics and Joint KAUST-HKUST Micro/Nanofluidics Laboratory, Hong Kong University of Science and Technology, Clear Water Bay, Hong Kong.*

Received 7 December 2010; Accepted (in revised version) 4 May 2011

Available online 28 October 2011

Abstract. We develop a continuum hydrodynamic model for two-phase immiscible flows that involve electroosmotic effect in an electrolyte and moving contact line at solid surfaces. The model is derived through a variational approach based on the Onsager principle of minimum energy dissipation. This approach was first presented in the derivation of a continuum hydrodynamic model for moving contact line in neutral two-phase immiscible flows (Qian, Wang, and Sheng, J. Fluid Mech. 564, 333–360 (2006)). Physically, the electroosmotic effect can be formulated by the Onsager principle as well in the linear response regime. Therefore, the same variational approach is applied here to the derivation of the continuum hydrodynamic model for charged two-phase immiscible flows where one fluid component is an electrolyte exhibiting electroosmotic effect on a charged surface. A phase field is employed to model the diffuse interface between two immiscible fluid components, one being the electrolyte and the other a nonconductive fluid, both allowed to slip at solid surfaces. Our model consists of the incompressible Navier-Stokes equation for momentum transport, the Nernst-Planck equation for ion transport, the Cahn-Hilliard phase-field equation for interface motion, and the Poisson equation for electric potential, along with all the necessary boundary conditions. In particular, all the dynamic boundary conditions at solid surfaces, including the generalized Navier boundary condition for slip, are derived together with the equations of motion in the bulk region. Numerical examples in two-dimensional space, which involve overlapped electric double layer fields, have been presented to demonstrate the validity and applicability of the model, and a few salient features of the two-phase immiscible electroosmotic flows at solid surface. The wall slip in the vicinity of moving contact line and the Smoluchowski slip in the electric double layer are both investigated.

PACS: 47.57.jd, 68.08.-p, 83.50.Rp, 83.10.Ff

Key words: Electroosmotic flow, moving contact line, slip boundary condition.

*Corresponding author. *Email addresses:* shaosihong@gmail.com (S. Shao), maqian@ust.hk (T. Qian)

1 Introduction

Recently, there have been rapid developments in the design, patterning, and utilization of microfluidic and nanofluidic devices which have found many applications in the devised transport, separation, identification, synthesis, and manipulation of a wide range of chemical and biological species [1]. In this respect, electroosmotic flows have been widely used to transport and mix fluids using electric fields in micro- and nanofluidic systems based on the lab-on-a-chip concept [2,3]. The use of mechanical pumps or valves with moving components is therefore avoided. When a solid wall is in contact with an electrolyte solution, it acquires a certain amount of charge on the surface through an electrochemical adsorption/desorption process, while the counterions are released from the solid surface into the solution. The electric double layer (EDL) is formed through an accumulation of the counterions in the solution adjacent to the wall. These excess counterions move under an external electric field and drag the fluid surrounding them. This electrokinetic effect causes a flow, termed as electroosmotic flow (EOF), in the bulk region via the viscous coupling. If the characteristic thickness of the EDL (i.e., the Debye length λ_D) is much smaller than the channel width (diameter), then the EOF will exhibit the plug-flow velocity profile, which is very different from the parabolic velocity profile in conventional pressure driven flows. Generally speaking, EOF is preferred for biomedical/chemical separation or detection applications since the plug-flow velocity profile reduces the sample dispersion effect, and consequently improve the device performance [4,5].

The fluid dynamics in confined geometries can be affected by the friction with confining walls. Theoretically, wall friction is quantified by setting some boundary conditions at the wall. The no-slip boundary condition, which states that there is no relative motion at the fluid-solid interface, has been extensively used and demonstrated in numerous macroscopic flows. However, over the past two decades, experiments have shown that slip occurs in mechanically driven flows over smooth solvophobic surfaces, with slip lengths typically of the order of nanometer [6]. Slip effects become increasingly important as the confinement space for fluids is reduced to sub-micrometer or nanometer scale. The flow enhancement due to slip could be up to two or three orders of magnitude [7,8]. Excellent reviews on the experimental and theoretical aspects of liquid slip can be found in [6,9]. This constitutes the first reason to explicitly take into account the wall slip in this work.

Research interests in the dynamics of two-phase fluids in narrow channels stem from many applications that microfluidic and nanofluidic devices have found in biological and chemical analyses, drug delivery, and chemical synthesis [10]. In particular, droplets of one fluid in the other immiscible fluid have been found useful in a wide range of applications, especially when the droplet size and the size distribution can be prescribed on a micro- or nanoscale [11]. Droplet generation, manipulation, and delivery within micro and nano systems have been extensively studied experimentally and numerically [12,13]. The flow phenomena in these applications constantly involve a classical problem in con-

tinuum fluid mechanics. Decades ago, it was discovered that in immiscible two-phase flows, the moving contact line (MCL), defined as the intersection of the fluid-fluid interface with the solid wall, is incompatible with the no-slip boundary condition [14–18]. Solving the equation of motion with the no-slip boundary condition in the vicinity of the MCL leads to a diverging stress and an infinite rate of energy dissipation. Actually, molecular dynamics (MD) simulations and experiments have shown that slip indeed occurs at the MCL [18]. This constitutes the second reason to model slip explicitly.

The recent discovery of the generalized Navier boundary condition (GNBC) [19, 20], which states that the amount of slipping is proportional to the sum of tangential viscous stress and the uncompensated Young stress, has resolved the MCL conundrum for two-phase immiscible flows. Numerical results of our continuum model have shown quantitative agreement with those from MD simulations [19, 20]. We would like to point out that by combining the GNBC with the diffuse-interface formulation, our model allows the coexistence of slip and diffusion, and in the systems in our MD simulations, it is slip that dominates. More recently, the GNBC has been variationally derived together with the equations of motion in the bulk region [21], through the principle of minimum energy dissipation as formulated by Onsager [22, 23]. This derivation means that the slip boundary condition at the fluid-solid interface is consistent with the general principle for irreversible thermodynamic processes. A recent study based on a sharp-interface model also demonstrated that the stress singularity is regularized by a slip region in the vicinity of the MCL where the Young stress is dominant [24].

In this paper, based on the variational approach presented in [21], we derive a continuum model for two-phase immiscible EOF that involve contact lines moving at solid surface. This model consists of the incompressible Navier-Stokes equation for momentum transport, the Nernst-Planck equation for ion transport, a phase-field equation of Cahn-Hilliard type for interface motion, and the Poisson equation for electric potential. In particular, the boundary conditions at solid surface are variationally derived together with the equations of motion in the bulk region, including the GNBC for slip at solid walls, a physical mechanism necessary for contact line motion. Our model is able to describe the coexistence of the apparent Smoluchowski slip in the EDL and the wall slip at the solid surface. Recently, it has been shown that wall slip is able to amplify the EOF [25] and hence enhance the electrokinetic energy conversion [26]. An accurate modeling of two-phase immiscible EOF is essential to the understanding of electrowetting [27, 28] (in which an external electric field is used to modify the wetting behavior of a conductive liquid in an insulating ambient fluid) and electrohydrodynamics [29–31] (in which the electric force due to the bounded charges at the interface can have a significant influence on the fluid motion and the interface stability). In addition, using a conductive fluid to pump a nonconductive fluid via viscous coupling is also an interesting application that involves two-phase immiscible EOF [4, 32]. The various flow phenomena mentioned above can in principle be studied using the present variational model.

The paper is organized as follows. There is a brief review of electroosmotic flows in Section 2. The variational derivation of the model is presented in Section 3. The numerical

results are presented with discussion in Section 4. The paper is concluded in Section 5 with a few remarks.

2 Electroosmotic flows

The Poisson (P) equation

$$\nabla\cdot\boldsymbol{D}=-\nabla\cdot(\epsilon\nabla V)=\rho_e \tag{2.1}$$

describes the relationship between the electric potential V and the net charge density ρ_e in the electrolyte solution. Here,

$$\boldsymbol{D}=\epsilon\boldsymbol{E}=-\epsilon\nabla V \tag{2.2}$$

is the electric displacement field and ϵ is the dielectric constant. If the electrolyte contains N ion species with charges eq_α and concentrations c_α ($\alpha=1,\cdots,N$, where e is the elementary charge and q_α is the valence of the α-th ion species), then $\rho_e=\sum_{\alpha=1}^{N}eq_\alpha c_\alpha$. Neglecting the effects of external and induced magnetic fields, we have the Nernst-Planck (NP) equation as the continuity equation for each ion species:

$$\frac{\partial c_\alpha}{\partial t}+\boldsymbol{v}\cdot\nabla c_\alpha=-\nabla\cdot\boldsymbol{J}_\alpha, \tag{2.3}$$

where $\boldsymbol{v}$ is the velocity of incompressible fluid and $\boldsymbol{J}_\alpha$ is the flux of the α-th ion species due to diffusion and electromigration, given by

$$\boldsymbol{J}_\alpha=-D_\alpha\nabla c_\alpha-eq_\alpha M_\alpha c_\alpha\nabla V. \tag{2.4}$$

Here D_α is the diffusion coefficient of the α-th ion species and M_α is the corresponding mobility, which is related to D_α through the Einstein relation $D_\alpha=M_\alpha k_BT$.

Consider a single-phase electrolyte confined between two parallel solid walls separated by a distance $2H$ in the z direction. The system has translational symmetry in the x direction. For the system in equilibrium, we have $\boldsymbol{J}_\alpha=0$, which gives

$$\frac{\mathrm{d}c_\alpha}{\mathrm{d}z}=-\frac{eq_\alpha c_\alpha}{k_BT}\frac{\mathrm{d}V}{\mathrm{d}z}, \tag{2.5}$$

describing the balance between osmotic pressure and electric force. In the classical theory for EDL, Eq. (2.5) is integrated from a point in bulk region where $z=\infty$, $V=0$, $c_\alpha=c_\alpha^0$ (i.e., the bulk concentration of the α-th ion species) to a point within the EDL. This leads to the Boltzmann equation

$$c_\alpha=c_\alpha^0\exp\left(-\frac{eq_\alpha V}{k_BT}\right). \tag{2.6}$$

For a symmetric unary electrolyte such as KCl and NaCl, the net charge density ρ_e is proportional to the local concentration difference between cations and anions, i.e.,

$$\rho_e=\sum_\alpha eq_\alpha c_\alpha=e(c_+-c_-)=-2ec^0\sinh\left(\frac{eV}{k_BT}\right), \tag{2.7}$$

with $q_+ = -q_- = 1$ and $c_+^0 = c_-^0 = c^0$. Substituting Eq. (2.7) into Eq. (2.1) and assuming the dielectric constant is spatially invariant, we obtain the well known Poisson-Boltzmann (PB) equation

$$\frac{\mathrm{d}^2 V}{\mathrm{d}z^2} = \frac{2ec^0}{\epsilon} \sinh\left(\frac{eV}{k_B T}\right). \tag{2.8}$$

If $eV/k_B T \ll 1$, then the right-hand side of Eq. (2.8) can be simplified using the Debye-Hückel approximation. This leads to

$$\frac{\mathrm{d}^2 V}{\mathrm{d}z^2} = \frac{V}{\lambda_D^2}, \tag{2.9}$$

where

$$\lambda_D = \sqrt{\frac{\epsilon k_B T}{2e^2 c^0}} \tag{2.10}$$

is called the Debye length, the characteristic thickness of EDL. The zeta potential ζ is defined as the potential difference between the confining wall and the centerline of the channel. Denoting the surface charge density on the wall by σ and using the electroneutrality condition, we can obtain the Grahame equation [33]

$$\zeta = \frac{2k_B T}{e} \sinh^{-1}\left(\frac{e\sigma\lambda_D}{2\epsilon k_B T}\right), \tag{2.11}$$

which describes the relation between ζ and σ under the assumption of $H \gg \lambda_D$, with the electric potential and its gradient vanishing far away from the wall.

In literature, the momentum transport in EOF is governed by the incompressible Navier-Stokes (NS) equation

$$\rho\left(\frac{\partial \boldsymbol{v}}{\partial t} + \boldsymbol{v}\cdot\nabla\boldsymbol{v}\right) = \eta\nabla^2\boldsymbol{v} - \nabla p - \rho_e \nabla V, \tag{2.12}$$

supplemented by the incompressibility condition $\nabla\cdot\boldsymbol{v} = 0$. Here ρ is the mass density, η is the shear viscosity, p is the pressure, and $-\rho_e\nabla V$ is the electric body force.

The PB-NS model has been extensively used in investigating the dynamics of EOF in microchannels [34–37]. However, it should be noted that the Boltzmann equation (2.6) is derived under the following assumptions [38]: (a) Ion distribution is stationary; (b) Convective transport of ions is negligible; (c) The two walls are separated far away from each other; (d) Variations of c_α and V only occur in the direction normal to the channel walls. If any of the above is violated, then the NP equation should be used instead. This leads to the fully coupled PNP-NS model. In [38], a model for determining the electric potential and ion concentration in the overlapped EDL is presented. An intermediate equilibrium state described by this model is further studied in a long nanopore with significant EDL overlap [39]. The NP equation is adopted instead of the Boltzmann equation to study the

convective effect due to inhomogeneous zeta potential in [40]. Obviously, for the two-phase immiscible flows illustrated in Fig. 1, the Boltzmann distribution is no longer a valid approximation. That is, we need to solve the NP equation (2.3) for ion concentrations. In general, the NP equation should be coupled with the Poisson equation (2.1) and the incompressible NS equation to simulate various flow phenomena, from the dynamics in [39–41] to the steady states in [38, 42–45].

Boundary conditions play a crucial role in modeling electrokinetic phenomena. Regarding the boundary condition for the Poisson equation, there are two different choices:

$$\boldsymbol{D}\cdot\boldsymbol{n}=-\sigma \tag{2.13}$$

for given surface charge density σ, and

$$V=\zeta \tag{2.14}$$

for given zeta potential ζ, where $\boldsymbol{n}$ is the outward pointing unit vector normal to the fluid-solid interface. The former equation is of the Neumann type while the latter of the Dirichlet type. These two boundary conditions have both been widely used. However, van der Heyden et al. [37] found that Eq. (2.14) with a constant zeta potential is invalid in calculating the variation of streaming conductance with salt concentration, while imposing a constant surface charge density in Eq. (2.13) yields good predictions at low salt concentration. In general, the chemical equilibrium model provides the best fit over the whole concentration range [37,46]. In this work, we will use the Neumann boundary condition (2.13) with the simple assumption of constant surface charge density, as adopted in [39, 43, 44, 47–49].

As to the hydrodynamic boundary conditions, the traditional no-slip condition is often used in solving the NS equation. However, recent theoretical studies have suggested a significant amplification of EOF over slippery surfaces [25, 26, 50]. Studies at molecular level have shown that the hydrodynamic boundary condition, for slip or no-slip, is determined by the molecular interactions between fluid and solid, and the channel size [51–53]. In the next section, we allow the fluid to slip at the solid surface and derive the slip boundary condition in a variational approach.

We also want to mention the celebrated Helmholtz-Smoluchowski (HS) slip velocity,

$$U_{eo}=-\frac{\epsilon\zeta E_0}{\eta}, \tag{2.15}$$

which gives the velocity in the bulk (far away from the solid boundary) for fully developed EOF driven by an applied electric field E_0. The HS velocity (2.15), derived from the balance between electric force and viscous force with the no-slip condition, relates the EOF velocity to the zeta potential and the applied electric field. For given ζ and E_0, U_{eo} is the velocity at large distances away from the wall (beyond the EDL), and hence the EOF shows the plug-like velocity profile.

3 Variational derivation of the model

3.1 The Cahn-Hilliard Navier-Stokes system with the GNBC

In the diffuse-interface modeling of binary fluids, a phase field $\phi(\boldsymbol{r})$ is introduced to measure the local relative concentration or composition in order to distinguish between the two fluid components [54]. It assumes distinct constant values in the two bulk components and undergoes a rapid but smooth transition in the interfacial region. The total free energy of the system $F[\phi(\boldsymbol{r})]$ consists of the Cahn-Hilliard (CH) free energy $F_{CH}[\phi(\boldsymbol{r})]$ which stabilizes the fluid-fluid interface and the surface free energy $F_{fs}[\phi(\boldsymbol{r})]$ which arises from the fluid-solid interactions:

$$F[\phi(\boldsymbol{r})]=F_{CH}[\phi(\boldsymbol{r})]+F_{fs}[\phi(\boldsymbol{r})], \tag{3.1}$$

where $F_{CH}[\phi(\boldsymbol{r})]$ and $F_{fs}[\phi(\boldsymbol{r})]$ are given by

$$F_{CH}[\phi(\boldsymbol{r})]=\int \mathrm{d}\boldsymbol{r}\left[\frac{K}{2}(\nabla\phi)^2+\left(-\frac{r}{2}\phi^2+\frac{u}{4}\phi^4\right)\right], \tag{3.2}$$

$$F_{fs}[\phi(\boldsymbol{r})]=\int \mathrm{d}S\left[\gamma_{fs}(\phi)\right]. \tag{3.3}$$

Here K, r and u are material parameters associated with the fluid-fluid interface, $\gamma_{fs}(\phi)$ is the free energy per unit area at the fluid-solid interface, and $\int \mathrm{d}S$ denotes the surface integral at the fluid-solid interface. The values of K, r and u are directly related to the fluid-fluid interfacial thickness $\xi=\sqrt{K/r}$, the interfacial tension $\gamma=2\sqrt{2}r^2\xi/3u$, and the two minima $\phi_\pm=\pm\sqrt{r/u}$ of the double well potential $-r\phi^2/2+u\phi^4/4$. In the previous MD simulations [19], ξ and γ can be measured and $\phi_\pm=\pm1$ for the two immiscible fluid components. For the free energy density at the fluid-solid interface, we use $\gamma_{fs}(\phi)=(\Delta\gamma_{fs}/2)\sin(\pi\phi/2)$, which is a smooth interpolation from $\gamma_{fs}(\phi_-)=-\Delta\gamma_{fs}/2$ (between fluid 1 and solid) to $\gamma_{fs}(\phi_+)=\Delta\gamma_{fs}/2$ (between fluid 2 and solid). Here $\Delta\gamma_{fs}$ denotes the change of $\gamma_{fs}(\phi)$ from ϕ_- to ϕ_+, i.e., $\Delta\gamma_{fs}=\gamma_{fs}(\phi_+)-\gamma_{fs}(\phi_-)$. According to the Young equation $\gamma_{fs}(\phi_-)=\gamma_{fs}(\phi_+)+\gamma\cos\theta_s$ with θ_s being the static contact angle, we have $\Delta\gamma_{fs}=-\gamma\cos\theta_s$ (in the partial wetting regime). Through the variational form of the total free energy

$$\delta\{F_{CH}[\phi(\boldsymbol{r})]+F_{fs}[\phi(\boldsymbol{r})]\}=\int \mathrm{d}\boldsymbol{r}(\mu_\phi\delta\phi)+\int \mathrm{d}S(L_\phi\delta\phi), \tag{3.4}$$

we define the chemical potential μ_ϕ in the bulk and the corresponding quantity L_ϕ at the fluid-solid interface:

$$\mu_\phi=-\nabla\cdot(K\nabla\phi)-r\phi+u\phi^3, \tag{3.5}$$

$$L_\phi=K\partial_n\phi-\frac{\sqrt{2}}{3}\frac{r^2\xi}{u}\cos\theta_s s_\gamma(\phi), \tag{3.6}$$

where $s_\gamma(\phi)=\frac{\pi}{2}\cos\frac{\pi\phi}{2}$. As ϕ is a conserved order parameter, the two-phase equilibrium conditions derived from minimizing $F_{CH}[\phi(\boldsymbol{r})]+F_{fs}[\phi(\boldsymbol{r})]$ are $\mu_\phi=$const. and $L_\phi=0$. Note that our choice of $\gamma_{fs}(\phi)$ makes $\partial\gamma_{fs}(\phi)/\partial\phi$ vanish at the two equilibrium phases $\phi_\pm=\pm1$. As a consequence, far away from the contact line and deep in the single-phase region, the phase field becomes a constant ($+1$ or -1) in space and time. This requirement can of course be met by other forms of $\gamma_{fs}(\phi)$, e.g., that adopted by Jacqmin [55] and Yue et al. [56]. The form in these two works does not distort the level curves in equilibrium and may lead to certain benefit in numerical simulations. We would like to pint out that though our choice leads to the contour distortion in phase field, the effect is however constrained at the contact line by the CH free energy in the bulk region.

Below we apply the Onsager principle of minimum energy dissipation [22, 23] to the derivation of our continuum model. For a system described by the variables $\{\alpha_1,\cdots,\alpha_N\}$ measuring the displacement from equilibrium, we need to construct a functional, hereafter denoted by A, for minimization with respect to $\{\dot{\alpha_1},\cdots,\dot{\alpha_N}\}$, the rates of change of the variables $\{\alpha_1,\cdots,\alpha_N\}$. There are two distinct parts in A: the dissipation function $\Phi=(1/2)\sum_{i,j}\eta_{ij}\dot{\alpha_i}\dot{\alpha_j}$, which is half the rate of free energy dissipation, being positive definite and quadratic in the rates $\dot{\alpha_i}$, and $\dot{F}=\sum_i(\partial F/\partial\alpha_i)\dot{\alpha_i}$, which is the rate of change of the free energy $F(\alpha_1,\cdots,\alpha_N)$. Here the damping coefficients η_{ij} satisfy the reciprocal relations $\eta_{ij}=\eta_{ji}$.

There are four distinct dissipative processes considered in the dissipation function Φ. The rate of dissipation due to the shear viscosity η in the bulk region is of the form

$$R_{vis}=\int \mathrm{d}\boldsymbol{r}\left[\frac{\eta}{2}(\partial_i v_j+\partial_j v_i)^2\right]. \tag{3.7}$$

The rate of dissipation due to the slip at solid surfaces is written as

$$R_{slip}=\int \mathrm{d}S[\beta(v_\tau^{slip})^2], \tag{3.8}$$

where v_τ^{slip} is the slip velocity, defined as the fluid velocity in the tangential (τ) direction relative to the solid at the fluid-solid interface, and β is the slip coefficient which has the dimension of [viscosity]/[length], from which the slip length l_s is defined as $l_s=\eta/\beta$. The no-slip boundary condition corresponds to the limit of $\beta\to\infty$. For the rate of dissipation due to the diffusion between the two fluid components, the relevant variable is the composition ϕ, a conserved order parameter satisfying the continuity equation

$$\dot{\phi}=\frac{\partial\phi}{\partial t}+\boldsymbol{v}\cdot\nabla\phi=-\nabla\cdot\boldsymbol{J}_\phi, \tag{3.9}$$

where $\boldsymbol{J}_\phi$ is the diffusive current density, which is taken as the rate variable here. Since the dissipation function must be quadratic in rates, we use

$$R_{diff}=\int \mathrm{d}\boldsymbol{r}\left(\frac{\boldsymbol{J}_\phi^2}{M_\phi}\right), \tag{3.10}$$

where M_ϕ is the mobility coefficient. At the fluid-solid interface, ϕ is no longer conserved. Consequently, $\dot{\phi}$ becomes the rate variable for the relaxational dynamics there, and the corresponding rate of dissipation is given by

$$R_{rel}=\int \mathrm{d}S\left(\frac{\dot{\phi}^2}{\Gamma}\right), \tag{3.11}$$

with Γ being a positive rate coefficient. The rate of dissipation due to the displacement from two-phase equilibrium is

$$R_\phi=R_{diff}+R_{rel}, \tag{3.12}$$

and the dissipation function is given by

$$\Phi=\frac{1}{2}(R_{vis}+R_{slip}+R_\phi). \tag{3.13}$$

As to the rate of change of the free energy $\dot{F}$, we replace $\delta\phi$ by $\partial\phi/\partial t=\dot{\phi}-\boldsymbol{v}\cdot\nabla\phi$ in Eq. (3.4) and obtain

$$\begin{aligned}\dot{F}&=\int \mathrm{d}\boldsymbol{r}\left(\mu_\phi\frac{\partial\phi}{\partial t}\right)+\int \mathrm{d}S\left(L_\phi\frac{\partial\phi}{\partial t}\right)\\&=\int \mathrm{d}\boldsymbol{r}\left[\mu_\phi(\dot{\phi}-\boldsymbol{v}\cdot\nabla\phi)\right]+\int \mathrm{d}S\left[L_\phi(\dot{\phi}-\boldsymbol{v}\cdot\nabla\phi)\right]\\&=\int \mathrm{d}\boldsymbol{r}\left(\nabla\mu_\phi\cdot\boldsymbol{J}_\phi-\mu_\phi\boldsymbol{v}\cdot\nabla\phi\right)+\int \mathrm{d}S\left(L_\phi\dot{\phi}-L_\phi v_\tau\partial_\tau\phi\right)\end{aligned} \tag{3.14}$$

using $\dot{\phi}=-\nabla\cdot\boldsymbol{J}_\phi$, $\boldsymbol{v}\cdot\boldsymbol{n}=0$ and $\boldsymbol{J}_\phi\cdot\boldsymbol{n}=0$ at the solid surface, together with an integration by parts $\int \mathrm{d}\boldsymbol{r}[\mu_\phi(-\nabla\cdot\boldsymbol{J}_\phi)]=\int \mathrm{d}\boldsymbol{r}(\nabla\mu_\phi\cdot\boldsymbol{J}_\phi)$.

According to the Onsager principle, we construct the functional A as $A=\Phi+\dot{F}$, which reads

$$\begin{aligned}A[\boldsymbol{v}(\boldsymbol{r}),\boldsymbol{J}_\phi(\boldsymbol{r}),\dot{\phi}(\boldsymbol{r})]=&\int \mathrm{d}\boldsymbol{r}\left(\frac{\boldsymbol{J}_\phi^2}{2M_\phi}\right)+\int \mathrm{d}\boldsymbol{r}\left(\nabla\mu_\phi\cdot\boldsymbol{J}_\phi\right)\\&+\int \mathrm{d}S\left(\frac{\dot{\phi}^2}{2\Gamma}\right)+\int \mathrm{d}S\left(L_\phi\dot{\phi}\right)\\&+\int \mathrm{d}\boldsymbol{r}\left[\frac{\eta}{4}(\partial_i v_j+\partial_j v_i)^2\right]+\int \mathrm{d}\boldsymbol{r}\left(-\mu_\phi\boldsymbol{v}\cdot\nabla\phi\right)\\&+\int \mathrm{d}S\left[\frac{\beta}{2}(v_\tau^{slip})^2\right]+\int \mathrm{d}S\left[-v_\tau(L_\phi\partial_\tau\phi)\right].\end{aligned} \tag{3.15}$$

Supplemented with the incompressibility condition $\nabla\cdot\boldsymbol{v}=0$, A is to be minimized with respect to the rates $\{\boldsymbol{v},\boldsymbol{J}_\phi,\dot{\phi}\}$. Minimizing A with respect to $\boldsymbol{J}_\phi$ yields the constitutive relation

$$\boldsymbol{J}_\phi=-M_\phi\nabla\mu_\phi, \tag{3.16}$$

which, in combination with the continuity equation, leads to the convection-diffusion equation

$$\frac{\partial\phi}{\partial t}+\boldsymbol{v}\cdot\nabla\phi=\nabla\cdot(M_\phi\nabla\mu_\phi). \tag{3.17}$$

Minimizing A with respect to $\dot{\phi}$ at the solid surface leads to the relaxational boundary condition

$$\frac{\partial\phi}{\partial t}+v_\tau\partial_\tau\phi=-\Gamma L_\phi. \tag{3.18}$$

In minimizing A with respect to $\boldsymbol{v}$, the incompressibility condition $\nabla\cdot\boldsymbol{v}=0$ is imposed via the use of a Lagrange multiplier $p(\boldsymbol{r})$ in an extra term $\int d\boldsymbol{r}(-p\nabla\cdot\boldsymbol{v})$. By writing the variation of A as the sum of a group of volume integrals and a group of surface integrals, we first obtain the Stokes equation

$$-\nabla p+\nabla\cdot\boldsymbol{\sigma}+\mu_\phi\nabla\phi=0, \tag{3.19}$$

with the Lagrange multiplier p being the pressure and $\boldsymbol{\sigma}=\eta[\nabla\boldsymbol{v}+(\nabla\boldsymbol{v})^T]$ the Newtonian viscous stress tensor, and then obtain the slip boundary condition

$$\beta v_\tau^{slip}=-\eta(\partial_n v_\tau+\partial_\tau v_n)+L_\phi\partial_\tau\phi, \tag{3.20}$$

where the slip coefficient $\beta=\beta(\phi)$, a function of the local composition, may vary from one fluid component to the other. The inertial effects are to be included by generalizing the Stokes equation to the NS equation with the capillary force

$$\rho\left(\frac{\partial\boldsymbol{v}}{\partial t}+\boldsymbol{v}\cdot\nabla\boldsymbol{v}\right)=\nabla\cdot\boldsymbol{\sigma}-\nabla p+\mu_\phi\nabla\phi. \tag{3.21}$$

Emerging from the application of the variational principle of Onsager, Eqs. (3.18) and (3.20) constitute a consistent pair and are denoted the generalized Navier boundary conditions (GNBC). Our continuum model for MCL in immiscible two-phase flows is formed by Eqs. (3.17), (3.18), (3.20), and (3.21), supplemented with the incompressibility condition $\nabla\cdot\boldsymbol{v}=0$ and the impermeability conditions $v_n=0$ and $\boldsymbol{J}_\phi\cdot\boldsymbol{n}=0$ at the solid surface.

3.2 Modeling the two-phase immiscible EOF

The hydrodynamics of two-phase immiscible EOF in narrow channels is modeled through the same variational approach outlined in Section 3.1. The flow geometry in our simulations is illustrated in Fig. 1. Here one fluid (fluid 1) is a conductive electrolyte and the other (fluid 2) is nonconductive, or both are electrolytes. For simplicity, we treat fluid 1 ($\phi=-1$) as an electrolyte and fluid 2 ($\phi=+1$) as a nonconductive fluid. The generalization to the case of two electrolytes is straightforward. We denote the cation concentration in the electrolyte by $c_1(\boldsymbol{r})$ and the anion concentration by $c_2(\boldsymbol{r})$. In the following, α is used to label the ion species with $\alpha=1,2$ and $\sum_\alpha$ means $\sum_{\alpha=1}^2$. We will employ a procedure

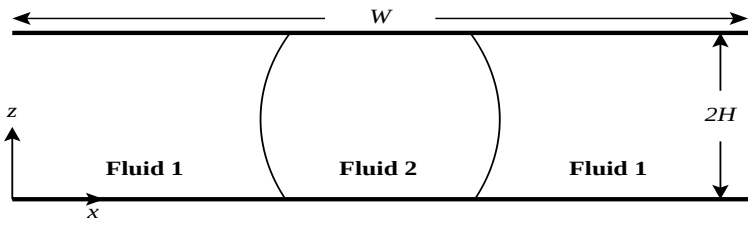

Figure 1: Two-dimensional (2D) simulations are carried out for EOF confined between two planar solid walls. For single-phase EOF, the whole channel is occupied by a conductive electrolyte. For two-phase EOF, the two curves denote the interfaces between an electrolyte (fluid 1) and a nonconductive fluid (fluid 2). The channel measures W in the x direction and $2H$ in the z direction. The origin of the coordinate system is at the lower left corner of the channel.

similar to that in Section 3.1 in order to derive the equations of motion in the bulk region and the relevant boundary conditions at solid surfaces simultaneously.

Compared to the neutral immiscible two-phase flows modeled in Section 3.1, the addition of ions leads to new contributions to both free energy and dissipation. In addition to the free energies F_{CH} in (3.2) and F_{fs} in (3.3), there are three new free energies to be included, for the entropy of ions, the electrostatic energy, and the ion-interface interaction. The first one is

$$F_{ent}[c_\alpha(\boldsymbol{r})]=\sum_\alpha\int \mathrm{d}\boldsymbol{r}(k_BTc_\alpha\ln c_\alpha), \tag{3.22}$$

which comes directly from entropy and drives the ion distribution toward a homogeneous state (of maximum entropy). The second one is the electrostatic energy

$$F_{es}[\phi(\boldsymbol{r}),c_\alpha(\boldsymbol{r})]=\int \mathrm{d}\boldsymbol{r}\left(\frac{1}{2}\boldsymbol{E}\cdot\boldsymbol{D}\right), \tag{3.23}$$

which depends on the dielectric constant $\epsilon(\phi)$ and the net charge density $\rho_e=\sum_\alpha eq_\alpha c_\alpha$ through Eqs. (2.1) and (2.2). Here all the effects of induced magnetic field are neglected and the electric fields are curl-free. The third one is the so called solvation free energy [47]

$$F_{sol}[\phi(\boldsymbol{r}),c_\alpha(\boldsymbol{r})]=\sum_\alpha\int \mathrm{d}\boldsymbol{r}(B_\alpha\phi c_\alpha), \tag{3.24}$$

which arises from the ion-interface interaction and plays the role of a phase-field barrier [57] that confines the ions within the electrolyte and keeps them from penetrating into the nonconductive fluid. For the case considered here, $\phi=-1$ and $+1$ correspond to the electrolyte and the nonconductive fluid, respectively. We choose $B_\alpha=B>0$ ($\alpha=1,2$) to set a barrier of height $2B$. In general, B should be large enough to prevent the ions from penetrating the fluid-fluid interface in the presence of an external electric field. The total free energy for two-phase immiscible EOF consists of five contributions as follows:

$$F[\phi(\boldsymbol{r}),c_\alpha(\boldsymbol{r})]=F_{CH}[\phi(\boldsymbol{r})]+F_{fs}[\phi(\boldsymbol{r})]+F_{ent}[c_\alpha(\boldsymbol{r})]+F_{es}[\phi(\boldsymbol{r}),c_\alpha(\boldsymbol{r})]+F_{sol}[\phi(\boldsymbol{r}),c_\alpha(\boldsymbol{r})]. \tag{3.25}$$

From Eqs. (2.1) and (2.2), we have the variational form [47]

$$\begin{aligned}\delta(\boldsymbol{E}\cdot\boldsymbol{D}) &= \delta(\epsilon\boldsymbol{E}^2)\\ &= -\boldsymbol{E}^2\delta\epsilon+2\boldsymbol{E}\cdot\delta\boldsymbol{D}\\ &= -\boldsymbol{E}^2\delta\epsilon-2\nabla\cdot(V\delta\boldsymbol{D})+2V\nabla\cdot\delta\boldsymbol{D}\\ &= -\boldsymbol{E}^2\delta\epsilon-2\nabla\cdot(V\delta\boldsymbol{D})+2eV\sum_\alpha q_\alpha\delta c_\alpha,\end{aligned}$$

from which we obtain the variation of the electrostatic energy

$$\delta\{F_{es}[\phi(\boldsymbol{r}),c_\alpha(\boldsymbol{r})]\} = -\int \mathrm{d}\boldsymbol{r}\left(\frac{1}{2}\boldsymbol{E}^2\delta\epsilon\right)+\int \mathrm{d}S(V\delta\sigma)+\sum_\alpha\int \mathrm{d}\boldsymbol{r}(eVq_\alpha\delta c_\alpha), \tag{3.26}$$

using the divergence theorem and the boundary condition (2.13).

We use a linear interpolation to define the dielectric constant in the interfacial region: $\epsilon(\phi)=\epsilon_1(1-\phi)/2+\epsilon_2(1+\phi)/2=\bar{\epsilon}+\tilde{\epsilon}\phi$ with $\bar{\epsilon}=(\epsilon_1+\epsilon_2)/2$ and $\tilde{\epsilon}=(\epsilon_2-\epsilon_1)/2$. This avoids introducing extra nonlinearity in the governing equations. For the free energy density at the fluid-solid interface, we use the nonlinear interpolation $\gamma_{fs}(\phi)=(\Delta\gamma_{fs}/2)\sin(\pi\phi/2)$ in Section 3.1 to ensure that L_ϕ vanishes at the two bulk equilibrium phases, i.e., $L_\phi(\phi)=0$ for $\phi=\pm1$. The nonlinear interpolation used for the surface charge density is $\sigma(\phi)=\sigma_1(1-\sin\frac{\pi\phi}{2})/2+\sigma_2(1+\sin\frac{\pi\phi}{2})/2$, which gives $\sigma(\phi)=\bar{\sigma}+\tilde{\sigma}\sin\frac{\pi\phi}{2}$, with $\bar{\sigma}=(\sigma_1+\sigma_2)/2$, $\tilde{\sigma}=(\sigma_2-\sigma_1)/2$, and the subscript i denoting the fluid component i ($i=1,2$). Substituting the above expressions for $\epsilon(\phi)$ and $\sigma(\phi)$ into Eq. (3.26), we obtain

$$\delta\{F_{es}[\phi(\boldsymbol{r}),c_\alpha(\boldsymbol{r})]\} = -\int \mathrm{d}\boldsymbol{r}\frac{\boldsymbol{E}^2}{2}\tilde{\epsilon}\delta\phi+\int \mathrm{d}SV\tilde{\sigma}\frac{\pi}{2}\cos\frac{\pi\phi}{2}\delta\phi+\sum_\alpha\int \mathrm{d}\boldsymbol{r}(eVq_\alpha\delta c_\alpha).$$

It is straightforward to obtain the variational form for each of the remaining terms in (3.25). The variation of the total free energy is of the form

$$\delta\{F[\phi(\boldsymbol{r}),c_\alpha(\boldsymbol{r})]\} = \int \mathrm{d}\boldsymbol{r}\left(\mu_\phi\delta\phi\right)+\int \mathrm{d}S\left(L_\phi\delta\phi\right)+\sum_\alpha\int \mathrm{d}\boldsymbol{r}(\mu_\alpha\delta c_\alpha),$$

in which μ_ϕ, L_ϕ, and μ_α are given by

$$\mu_\phi = -\nabla\cdot(K\nabla\phi)-r\phi+u\phi^3+\sum_\alpha B_\alpha c_\alpha-\frac{\tilde{\epsilon}}{2}(\nabla V)^2, \tag{3.27}$$

$$L_\phi = K\partial_n\phi+\left(V\tilde{\sigma}-\frac{\sqrt{2}}{3}\frac{r^2\xi}{u}\cos\theta_s\right)s_\gamma(\phi), \tag{3.28}$$

$$\mu_\alpha = k_BT(\ln c_\alpha+1)+eq_\alpha V+B_\alpha\phi,\quad \alpha=1,2. \tag{3.29}$$

Here μ_ϕ and L_ϕ have been redefined and μ_α is defined as the chemical potential for c_α. The equilibrium conditions derived from minimizing the free energy $F[\phi(\boldsymbol{r}),c_\alpha(\boldsymbol{r})]$ given

in Eq. (3.25) are μ_ϕ=const., L_ϕ=0, and μ_α=const.. It is readily seen that deviation from the equilibrium is measured by $\nabla\mu_\phi$ and $\nabla\mu_\alpha$ in the bulk, and L_ϕ at the fluid-solid interface. It follows that for small perturbations away from the equilibrium, there is a new rate of dissipation R_c in addition to those included in the rate of dissipation R_ϕ given in Eq. (3.12). Arising from the spontaneous response to the inhomogeneity of μ_α, R_c is given by

$$R_c=\sum_\alpha\int \mathrm{d}\boldsymbol{r}\left(\frac{\boldsymbol{J}_\alpha^2}{c_\alpha M_\alpha}\right), \tag{3.30}$$

in which the current density $\boldsymbol{J}_\alpha$ of ions is taken as the rate variable, and M_α is the corresponding mobility coefficient. The total dissipation function for two-phase immiscible EOF is given by

$$\Phi=\frac{1}{2}(R_{vis}+R_{slip}+R_\phi+R_c). \tag{3.31}$$

Following a procedure similar to that for deriving Eq. (3.14) in Section 3.1, we have the rate of change of the total free energy

$$\dot{F}=\int \mathrm{d}\boldsymbol{r}\left(\nabla\mu_\phi\cdot\boldsymbol{J}_\phi-\mu_\phi\boldsymbol{v}\cdot\nabla\phi\right)+\int \mathrm{d}S\left(L_\phi(\dot{\phi}-v_\tau\partial_\tau\phi)\right)+\sum_\alpha\int \mathrm{d}\boldsymbol{r}(\nabla\mu_\alpha\cdot\boldsymbol{J}_\alpha-\mu_\alpha\boldsymbol{v}\cdot\nabla c_\alpha),$$

in which the continuity equation (2.3) for ion concentration has been used with the boundary condition $\boldsymbol{J}_\alpha\cdot\boldsymbol{n}=0$ at the solid surface. Then we construct the functional A as

$$A[\boldsymbol{v},\boldsymbol{J}_\phi,\boldsymbol{J}_1,\boldsymbol{J}_2,\dot{\phi}]=\Phi+\dot{F}+\int \mathrm{d}\boldsymbol{r}(-\tilde{p}\partial_i v_i), \tag{3.32}$$

which is to be minimized with respect to the rates $\{\boldsymbol{v},\boldsymbol{J}_\phi,\boldsymbol{J}_\alpha,\dot{\phi}\}$ (α=1,2).

Minimizing A with respect to $\boldsymbol{v}$, we obtain the Stokes equation

$$\nabla\cdot\boldsymbol{\sigma}-\nabla\tilde{p}+\mu_\phi\nabla\phi+\sum_\alpha\mu_\alpha\nabla c_\alpha=0,$$

and the slip boundary condition as expressed in Eq. (3.20) but with L_ϕ redefined in Eq. (3.28). To show the effects of electric field more clearly, we introduce $p=\tilde{p}-\sum_\alpha c_\alpha\mu_\alpha$ as the new pressure and then make use of the expression for μ_α in Eq. (3.29). The Stokes equation becomes

$$\nabla\cdot\boldsymbol{\sigma}-\nabla p+\left[\mu-\frac{\tilde{\varepsilon}\boldsymbol{E}^2}{2}\right]\nabla\phi-k_BT\sum_\alpha\nabla c_\alpha+\rho_e\boldsymbol{E}=0, \tag{3.33}$$

with $\mu=-\nabla\cdot(K\nabla\phi)-r\phi+u\phi^3$. By including the acceleration terms, the Stokes equation is immediately generalized to the NS equation

$$\rho\left(\frac{\partial\boldsymbol{v}}{\partial t}+\boldsymbol{v}\cdot\nabla\boldsymbol{v}\right)=\nabla\cdot\boldsymbol{\sigma}-\nabla p+\mu\nabla\phi-\frac{\tilde{\varepsilon}\boldsymbol{E}^2}{2}\nabla\phi-k_BT\sum_\alpha\nabla c_\alpha+\rho_e\boldsymbol{E}. \tag{3.34}$$

A comparison with Eq. (2.12) shows that there are three extra terms appearing in Eq. (3.34). They are $\mu\nabla\phi$ for the capillary force, $-\frac{\tilde{\varepsilon}}{2}\boldsymbol{E}^2\nabla\phi$ due to the Maxwell stress, and $-k_BT\sum_\alpha\nabla c_\alpha$ due to the osmotic pressure gradient (which is missing in Eq. (2.12)). Comparing Eq. (3.34) with Eq. (3.21), we see that the last three terms in the right-hand side of Eq. (3.34) are included for electrokinetic effect.

Minimizing A with respect to $\boldsymbol{J}_\alpha$ yields

$$\boldsymbol{J}_\alpha=-c_\alpha M_\alpha\nabla\mu_\alpha=-D_\alpha\nabla c_\alpha-eq_\alpha M_\alpha c_\alpha\nabla V-M_\alpha B_\alpha c_\alpha\nabla\phi, \tag{3.35}$$

which, in combination with the continuity equation (2.3), leads to the NP equation. A comparison of Eq. (3.35) with Eq. (2.4) shows that the last term in the right-hand side of Eq. (3.35), which arises from the solvation free energy (3.24), reflects the blocking effect of fluid-fluid interface on ion transport.

Minimizing A with respect to $\boldsymbol{J}_\phi$ and $\dot{\phi}$, we obtain equations (3.16) and (3.18), respectively, but with μ_ϕ and L_ϕ redefined in (3.27) and (3.28). It is noted that $\tilde{\sigma}$, which denotes the surface charge density difference, appears explicitly in the surface quantity L_ϕ in (3.28). This indicates that $\tilde{\sigma}$ would affect both the slip and the relaxation at the fluid-solid interface.

In summary, our variational model for two-phase immiscible EOF consists of the following governing equations

- (2.1) for electric potential V (the Poisson equation),
- (2.3) and (3.35) for ion transport (the Nernst-Planck equation),
- (3.17) for phase field (i.e., fluid-fluid interface movement) (the Cahn-Hilliard equation),
- (3.34) for momentum transport (the Navier-Stokes equation),
- the incompressibility condition $\nabla\cdot\boldsymbol{v}=0$,

with the boundary conditions at the fluid-solid interface

- $\partial_n V=\sigma/\epsilon$,
- $\partial_n\mu_\alpha=0$,
- the relaxational boundary condition (3.18) and $\partial_n\mu_\phi=0$,
- the slip boundary condition (3.20) for tangential velocity and $v_n=0$ for normal velocity.

Here, μ_ϕ, L_ϕ, and μ_α are expressed in Eqs. (3.27), (3.28), and (3.29), respectively.

A phase-field model has recently been presented for electrowetting [28] through a similar variational approach. Our model is different from that model in the following sense:

1. We use two concentrations c_α for cations and anions to describe the ion distribution and transport, rather than a single change density as in [28]. This is essential to an accurate description of the structure of EDL and the Smoluchowski slip therein, to be demonstrated in our simulations for single-phase EOF. In our free energy expression, $F_{ent}[c_\alpha(\boldsymbol{r})]$ comes from entropy. It leads to the osmotic pressure gradient $-k_BT\sum_\alpha \nabla c_\alpha$ in the momentum equation and the diffusive flux in ion transport. There is a similar term in the free energy in [28], in the form of $F_\rho = \frac{\lambda}{2}\int_\Omega \rho^2$, where λ is a small coefficient, ρ the charge density, and Ω the spatial domain in which the fluids are contained. It seems to us that there is a reminiscence of entropy in F_ρ, which is minimized by uniform charge distribution (subject to charge conservation).

2. The surface charge density σ appears explicitly in our model, from the boundary condition for the Poisson equation to the variation of electrostatic energy. We note that the surface charge density σ is essential to the formation of EDL, in both physical reality and mathematical formulation.

3. In our free energy expression, the solvation free energy $F_{sol}[\phi(\boldsymbol{r}),c_\alpha(\boldsymbol{r})]$ is introduced to prevent ions from penetrating through the fluid-fluid interface into the nonconductive fluid. Such a mechanism is absent in [28].

Numerical results presented in Section 4 will show that (a) an accurate modeling of the EDL necessitates two concentrations for cations and anions, and the surface charge density as well; (b) under an applied bias field, the solvation free energy leads to a gradual redistribution of charge from the EDL to a layer next to the fluid-fluid interface; (c) numerical implementation with the GNBC leads to the amplification of EOF by wall slippage and the partial slip around the MCL. It is noted that in [28], although the slip boundary condition is derived, the numerical examples are still presented with the no-slip condition.

It's worth pointing out that while phase-field models can introduce a regularization to remove the non-integrable stress singularity in the neighborhood of the MCL with the no-slip boundary condition, the role of fluid slip at solid walls still needs to be taken into account explicitly, especially when the flow has a characteristic length down to the submicrometer or nanometer scale [19, 21, 24]. The microscopic mechanism (diffusion across fluid-fluid interfaces or slip at solid surfaces) has a significant effect on the flow in the vicinity of the MCL (i.e., the inner solution).

3.3 Dimensionless equations

Our variational model is phenomenological and involves many parameters. They are ρ and η in the momentum equation, K, r, and u in the Cahn-Hilliard free energy for the fluid-fluid interface (with $\xi = \sqrt{K/r}$ being the length scale for interfacial thickness), M_ϕ and Γ for the evolution of ϕ, B_α, D_α and $M_\alpha = D_\alpha/k_BT$ for the transport of ions, the permittivity ϵ, and the slip length l_s. Introducing the reference quantities L_{ref} for length, U_{ref}

for velocity, C_{ref} for concentration, and E_{ref} for electric field, we can nondimensionalize the governing equations with the dimensionless variables defined as follows:

$$\begin{aligned}
&\boldsymbol{r}=\boldsymbol{r}'L_{ref}, \qquad \boldsymbol{v}=\boldsymbol{v}'U_{ref}, \qquad t=t'\frac{L_{ref}}{U_{ref}}, \qquad p=p'\frac{\eta U_{ref}}{L_{ref}},\\
&c_\alpha=c'_\alpha C_{ref}, \qquad \boldsymbol{E}=\boldsymbol{E}'E_{ref}, \qquad V=V'L_{ref}E_{ref}, \qquad \sigma=\sigma' eL_{ref}C_{ref}.
\end{aligned}$$

The values of the above model parameters and reference quantities are listed in Table 1. Dropping the primes denoting dimensionless quantities, we have the nondimensionalized system consisting of the bulk equations

$$\begin{aligned}
&\nabla\cdot(\mathcal{E}(\phi)\nabla V)=\sum_\alpha q_\alpha c_\alpha,\\
&\frac{\partial c_\alpha}{\partial t}+\boldsymbol{v}\cdot\nabla c_\alpha=\mathcal{D}_\alpha\nabla^2 c_\alpha+\mathcal{P}_\alpha q_\alpha\nabla\cdot(c_\alpha\nabla V)+\mathcal{C}_\alpha\nabla\cdot(c_\alpha\nabla\phi), \quad (\alpha=1,2),\\
&\frac{\partial\phi}{\partial t}+\boldsymbol{v}\cdot\nabla\phi=\mathcal{L}_d\nabla^2\mu+\sum_\alpha\mathcal{L}_\alpha\nabla^2 c_\alpha-\mathcal{L}_e\nabla^2(\nabla V)^2,\\
&\mathcal{R}\left(\frac{\partial\boldsymbol{v}}{\partial t}+\boldsymbol{v}\cdot\nabla\boldsymbol{v}\right)=-\nabla p+\nabla^2\boldsymbol{v}+[\mathcal{B}\mu-\mathcal{Q}(\nabla V)^2]\nabla\phi-\mathcal{S}\sum_\alpha\nabla c_\alpha-\mathcal{F}\left(\sum_\alpha q_\alpha c_\alpha\right)\nabla V,
\end{aligned}$$

and the GNBC at the solid surface

$$\begin{aligned}
&(\mathcal{L}_s(\phi))^{-1}v_\tau^{slip}=\mathcal{B}L\partial_\tau\phi-\partial_n v_\tau+\mathcal{F}V\tilde{\sigma}s_\gamma(\phi)\partial_\tau\phi,\\
&\frac{\partial\phi}{\partial t}+v_\tau\partial_\tau\phi=-\mathcal{V}_s L-\mathcal{V}_e V\tilde{\sigma}s_\gamma(\phi),
\end{aligned}$$

with $\mu=-\nabla^2\phi-\phi+\phi^3$ and $L=\partial_n\phi-\frac{\sqrt{2}}{3}\cos\theta_s s_\gamma(\phi)$. The dimensionless parameters appearing in the above system are given by

$$\begin{aligned}
&\mathcal{R}=\frac{\rho\xi U_{ref}}{\eta}, \quad \mathcal{B}=\frac{r\xi}{\eta U_{ref}}, \quad \mathcal{Q}=\frac{\tilde{\epsilon}\xi E_{ref}^2}{2\eta U_{ref}}, \quad \mathcal{S}=\frac{k_B T\xi C_{ref}}{\eta U_{ref}},\\
&\mathcal{F}=\frac{e\xi^2 C_{ref}E_{ref}}{\eta U_{ref}}, \quad \mathcal{L}_d=\frac{rM_\phi}{\xi U_{ref}}, \quad \mathcal{L}_\alpha=\frac{B_\alpha M_\phi C_{ref}}{\xi U_{ref}}, \quad \mathcal{L}_e=\frac{\tilde{\epsilon}M_\phi E_{ref}^2}{2\xi U_{ref}},\\
&\mathcal{D}_\alpha=\frac{D_\alpha}{\xi U_{ref}}, \quad \mathcal{P}_\alpha=\frac{eD_\alpha E_{ref}}{k_B T U_{ref}}, \quad \mathcal{C}_\alpha=\frac{B_\alpha D_\alpha}{k_B T\xi U_{ref}}, \quad \mathcal{E}(\phi)=\frac{\epsilon(\phi)E_{ref}}{e\xi C_{ref}},\\
&\mathcal{L}_s(\phi)=\frac{\eta}{\beta(\phi)\xi}, \quad \mathcal{V}_s=\frac{K\Gamma}{U_{ref}}, \quad \mathcal{V}_e=\frac{\mathcal{V}_s\mathcal{F}}{\mathcal{B}}=\frac{e\xi^3\Gamma C_{ref}E_{ref}}{U_{ref}}.
\end{aligned}$$

Table 1: Parameters and values.

Symbol	Description	Value
ρ	mass density	$10^3\text{kg}\cdot\text{m}^{-3}$
η	shear viscosity	$10^{-3}\text{kg}\cdot\text{m}^{-1}\cdot\text{s}^{-1}$
r and u	fluid-fluid interfacial parameters	$5.3\times10^7\text{J}\cdot\text{m}^{-3}$
$\xi=\sqrt{K/r}$	fluid-fluid interfacial thickness	10^{-9}m
M_ϕ	mobility coefficient for ϕ	$3.8\times10^{-17}\text{m}^3\cdot\text{s}\cdot\text{kg}^{-1}$
Γ	rate coefficient for ϕ	$3.8\times10^{10}\text{s}\cdot\text{kg}^{-1}$
B	energy barrier for ion confinement	$1.85\times10^{-19}\text{J}$
D	diffusion constant for ions	$2\times10^{-9}\text{m}^2\cdot\text{s}^{-1}$
T	temperature	298.15K
ϵ	permittivity	$7.08\times10^{-10}\text{F}\cdot\text{m}^{-1}$
l_s	slip length	$5\times10^{-10}\text{m}$
L_{ref}	length unit	10^{-9}m
U_{ref}	velocity unit	$30\text{m}\cdot\text{s}^{-1}$
C_{ref}	concentration unit	$1\text{mol}\cdot\text{m}^{-3}$(=1mM)
E_{ref}	field strength unit	$10^9\text{V}\cdot\text{m}^{-1}$

4 Results and discussion

To obtain numerical solutions for the model, we use a pressure-Poisson solver for the NS equation [58], a semi-implicit scheme for the CH equation [59], and a conservative finite difference method for the NP equation [60]. The numerical method adopted here is mostly the same as that in [19]. In this section, we first present the setup of the simulated systems, including the relevant parameters, initial conditions, and boundary conditions. We then carry out single-phase EOF simulations. This is to show some finite-size effects and to (partially) verify the validity of our numerical implementation. In our two-phase EOF simulations, we focus on the flow phenomena with an interplay between the microscopic slip at the solid surface and the apparent slip accumulated in the EDL. We also present results for charge transport and the effects of contact angle.

4.1 Setup

As illustrated in Fig. 1, simulations are carried out for flows in a two-dimensional (2D) channel with the length W and the height $2H$. The model parameters are listed in Table 1. Here the same material parameters are used for the electrolyte (fluid 1) and the dielectric fluid (fluid 2), including the mass density, viscosity, and permittivity. The same diffusion coefficient D and barrier height B are used for cations and anions. The interfacial tension $\gamma=\frac{2\sqrt{2}}{3}\frac{r^2\xi}{u}\simeq50\text{mN}\cdot\text{m}^{-1}$ is comparable to that between the mineral oil and water [61]. The surface charge density at the electrolyte-solid interface is set to be $\sigma_1=-2\times10^{-3}\text{C}\cdot\text{m}^{-2}$, while $\sigma_2=0$ for the dielectric fluid means that there is no surface charge at the other fluid-solid interface.

In the x direction, periodic boundary conditions are used for the order parameter ϕ, fluid velocity $\boldsymbol{v}=(v_x,v_z)$, and ion concentrations c_α, while a Neumann-type boundary condition

$$-\frac{\partial V}{\partial x}=E_0 \tag{4.1}$$

is used for the electric potential V to apply the bias field $\boldsymbol{E}_0\hat{\boldsymbol{x}}$.

The simulation is divided into two steps. In the first step, we compute the equilibrium state without bias field (i.e., $E_0=0$) from a profile with two planer interfaces for ϕ and a uniform distribution of ions. The initial conditions are

$$\phi(x,z;t=0)=\begin{cases}\tanh\frac{x-x_l}{\sqrt{2}\tilde{\xi}}, & x\le(x_l+x_r)/2,\\ -\tanh\frac{x-x_r}{\sqrt{2}\tilde{\xi}}, & x>(x_l+x_r)/2,\end{cases} \tag{4.2}$$

$$c_1(x,z;t=0)=\left(c^0-\frac{\sigma_1}{eH}\right)\frac{1-\phi(x,z;t=0)}{2}, \tag{4.3}$$

$$c_2(x,z;t=0)=c^0\frac{1-\phi(x,z;t=0)}{2}, \tag{4.4}$$

where x_l (x_r) is the location of the interface on the left (right), c^0 is the bulk concentration, and $\Delta c=-\sigma_1/eH$ is required by the overall electroneutrality condition

$$\sigma_1+\int_0^H \rho_e \mathrm{d}z=0, \tag{4.5}$$

which is also called the compatibility condition for the Poisson equation (2.1). Due to the symmetry of the system, simulations are carried out in the lower half of the channel, i.e., $[0,L]\times[0,H]$, with the symmetry boundary conditions applied at the middle level $z=H$. The dimensionless Poisson-Nernst-Planck-Cahn-Hilliard system without fluid velocity is solved until the rate of change falls below a given tolerance, say, 10^{-6} here. In the second step, we turn on the bias field in the x direction to induce the EOF. The flow phenomena are investigated over a long time interval.

4.2 Single-phase EOF

Partly as a calibration, numerical results are obtained for single-phase EOF, in which ϕ remains at $\phi=-1$ for the electrolyte. We use $c^0=1$mM for the bulk concentration of ions and $\sigma_1=-2\times10^{-3}\mathrm{C}\cdot\mathrm{m}^{-2}$ for the surface charge density. Correspondingly, the Debye length defined in (2.10) is $\lambda_D\simeq9.711$nm and the zeta potential ζ_G given by the Grahame equation (2.11) is $\zeta_G\simeq-26.26$mV. Since the present model employs the NP equation to describe the ion distribution and transport, we can investigate the electric potential and ion concentrations for both $H\sim\lambda_D$ with overlapped EDL fields and $H\gg\lambda_D$ without overlapped EDL fields.

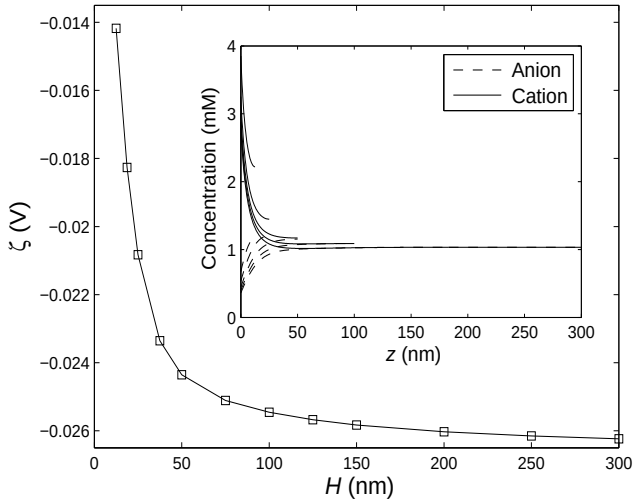

Figure 2: Zeta potential ζ in single-phase EOF, defined as the potential variation from $z=H$ to $z=0$ at equilibrium, is plotted as a function of H. The inset shows the ion concentrations for $H=12.5,25,50,100,300$.

We first set $E_0=0$ and find the equilibrium states for different channel heights. In Fig. 2, we plot the zeta potential ζ, here defined as the potential variation from $z=H$ to $z=0$, as a function of H, half of the channel height. The ζ-H curve shows a strong H dependence for small H, with ζ approaching $\zeta_G\simeq -26.26$mV predicted by the Grahame equation (2.11) as $H\to\infty$. Actually, the zeta potential for H=300 agree with the prediction of the Grahame equation in the first four figures after the decimal point. The inset of Fig. 2 shows the ion concentrations for different values of H. It is observed that (a) for very small channel height (in comparison with λ_D) with overlapped EDL fields, the channel is mostly a unipolar solution of cations that neutralizes the negative surface charge [43]; (b) for large channel height without overlapped EDL fields, the cations and anions have nearly the same concentration (i.e., c^0) far away from the wall.

We then turn on the bias electric field $E_0=10^6\text{V}\cdot\text{m}^{-1}$. The steady state is obtained by marching the dimensionless Poisson-Nernst-Planck-Navier-Stokes system until the relative change between two successive time steps is less than a given tolerance, say, 10^{-6} here. To show the electrokinetic effect in confined geometry, the velocity is measured by U_{eo} defined in (2.15) with $\zeta=\zeta_G$. Here the Navier slip boundary condition is used with the slip length given by l_s=0.5nm. In Fig. 3, we plot the flow rate $Q=H^{-1}\int_0^H v_x(z)\text{d}z$ as a function of H. It is seen that Q increases with the increasing H and approaches a constant as $H\to\infty$, thus indicating the plug-flow profiles plotted in the inset of Fig. 3. It is also observed that (a) the average velocity and the maximum velocity both increase with the channel height; (b) plug-flow profile becomes more obvious for larger channel height; (c) the flow enhancement due to slip is confirmed. For $H=300$, the factor is about 1.05, in agreement with the theoretical prediction $1+l_s/\lambda_D$ [7,8].

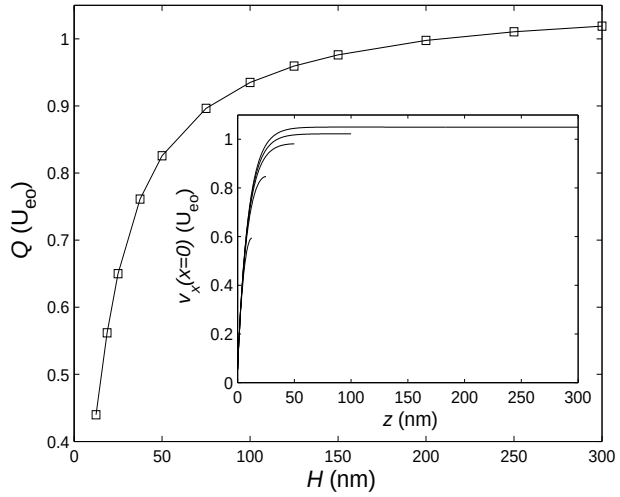

Figure 3: Flow rate $Q=H^{-1}\int_0^H v_x(z)\mathrm{d}z$ in single-phase EOF is plotted as a function of H for steady states. The inset shows the velocity profiles $v_x(z)$ at $x=0$ for $H=12.5,25,50,100,300$.

To summarize, the above results show that our numerical calculations that involve the Poisson equation, Nernst-Planck equation, and Navier-Stokes equation with the Navier boundary condition can reach high accuracy, with or without overlapped EDL fields. As for the Cahn-Hilliard equation, the method is the same as that in [19,21], with its accuracy already demonstrated. Below we use the same codes to simulate two-phase EOF.

4.3 Two-phase EOF

Initially, the nonconductive fluid 2 is located in the central region of the channel, with an extension $W_0=|x_r-x_l|$ in the x direction. The rest of the space is occupied by fluid 1, the electrolyte. In the simulation results presented below, the initial extension of fluid 2 is fixed at $W_0=25$nm, H is fixed at 25nm, the velocity is measured by U_{eo} defined in (2.15) with $\zeta=\zeta_G$ given by the Grahame equation (2.11), and the time unit is $1/30$ns. For simple Lennard-Jones liquids, continuum hydrodynamic formulation has been found valid for channels of width as small as a few tens of σ_{LJ}, the length parameter in the Lennard-Jones potential [19, 20]. This indicates that the continuum formulation can still be used for channel width $2H=50$nm. What makes the issue more complicated is the addition of ions in the present study as it is usually very difficult for a continuum formulation to take into account the steric effects due to the finite size of ions. Bearing this in mind, we have to assume that the ion size is at most comparable to the size of solvent molecules.

4.3.1 $\theta_s=90^\circ$

We start from the static contact angle $\theta_s=90^\circ$ with the static fluid-fluid interfaces perpendicular to the solid walls. In Fig. 4, we plot the fluid velocity at the center of the left

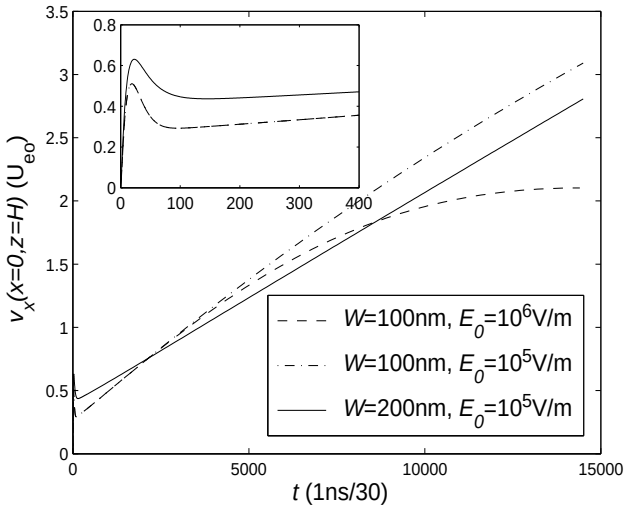

Figure 4: v_x at $(x=0,z=H)$ (the center of the left boundary of the channel) plotted as a function of time. The inset is an enlarged view for the initial stage from $t=0$ to 400, with the two curves for case (1) and case (2) being indistinguishable.

boundary of the channel as a function of time for three different cases: (1) $W=100$nm, $E_0=10^6$V/m; (2) $W=100$nm, $E_0=10^5$V/m; (3) $W=200$nm, $E_0=10^5$V/m. In case (1), $v_x(0,H)$ shows a fast increase in the beginning and reaches the local maximum 0.510 at $t=20$. Then it decreases to the local minimum 0.292 at $t=97$. After that, it shows a slow increase over a long time interval and reaches the steady value 2.103 at about $t=14000$. As to the other two cases, similar behaviors are observed though more time is needed for $v_x(0,H)$ to reach the steady value. In the inset of Fig. 4, the initial stage is better viewed for from $t=0$ to 400. It is seen that the two curves for case (1) and case (2) are indistinguishable. This indicates that in the initial stage, the velocity field is proportional to the applied bias field according to the initial charge distribution. (Note that $v_x(0,H)$ is measured by U_{eo} which is also $\propto E_0$.) In this stage, the driving force comes from the charged EDL. It takes a long time to reach the final steady state due to the slow charge transport. Initially, the charge is concentrated in the EDL next to the solid walls. Due to the slow transport in the flow, the charge gradually accumulates next to the fluid-fluid interfaces, with positive charge on the left of the left interface and negative charge on the right of the right interface, as shown in Fig. 5, as the applied field is in the $+x$ direction. It is noted that case (1) and case (2) have the same initial charge distribution but different strengths of applied electric field. Therefore, charge transport is slower in case (2) than in case (1) and hence it takes much longer time to reach the steady state, as indicated in Fig. 4. As for case (3), W is doubled and hence the approach to the steady state is even slower.

The time variation of charge distribution is closely related to that of the flow field. The profiles of v_x at the left boundary $x=0$ (the inlet) at different time instants are shown in Fig. 6. In the initial stage (from $t=0$ to $t=400$), the driving force on the fluid is con-

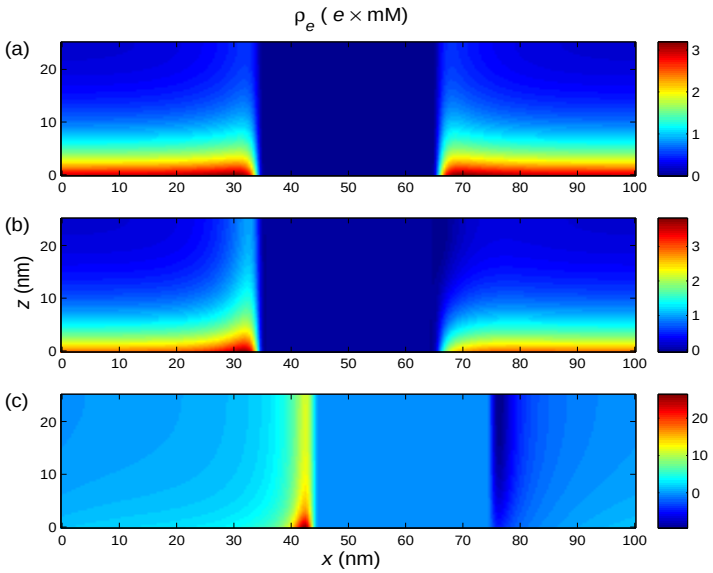

Figure 5: The net charge density fields for case (1) at (a) $t=0$, (b) $t=400$, and (c) $t=14338$. In (a) and (b), the charge is concentrated in the EDL next to the solid surface. Due to the slow transport in the flow, the charge gradually accumulates next to the fluid-fluid interfaces, as shown in (c).

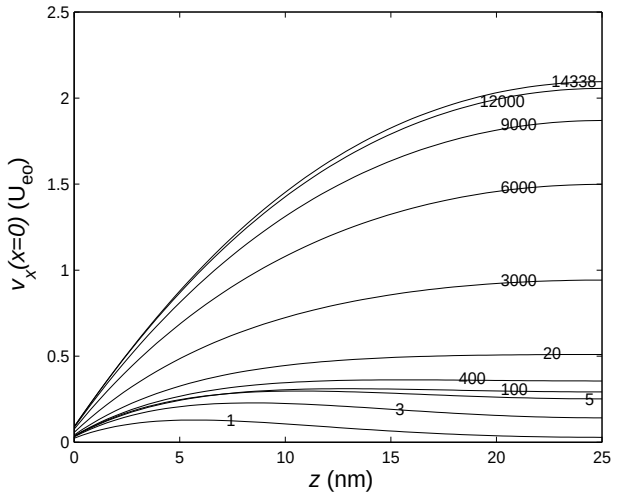

Figure 6: v_x plotted as a function of z at the left boundary $x=0$ for case (1). Different curves correspond with different time instants marked on the curves. Note that the time variation of $v_x(0,H)$ shown here corresponds with that in Fig. 4.

centrated in the EDL next to the solid walls. Consequently, the EOF is started near the confining walls and soon approaches the plug-flow profile, as shown by the curves at $t=1,3,5,20,100,400$ in Fig. 6. After that, there is a slow charge redistribution over a long time interval. As the charge is concentrated near the fluid-fluid interfaces finally, the

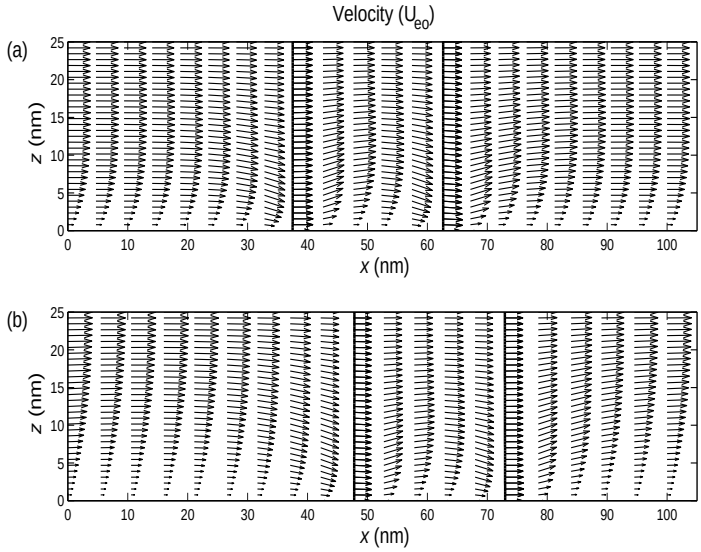

Figure 7: The velocity fields for case (1) at (a) $t=400$ and (b) $t=14338$. The thick solid lines represent the fluid-fluid interfaces determined by $\phi=0$. Far away from the fluid-fluid interfaces, the flow shows plug-flow profile in (a) but parabolic profile in (b), due to distinct charge distributions. The interfaces are flat because of the very small capillary number $\eta U_{eo}/\gamma \sim 4\times 10^{-4}$.

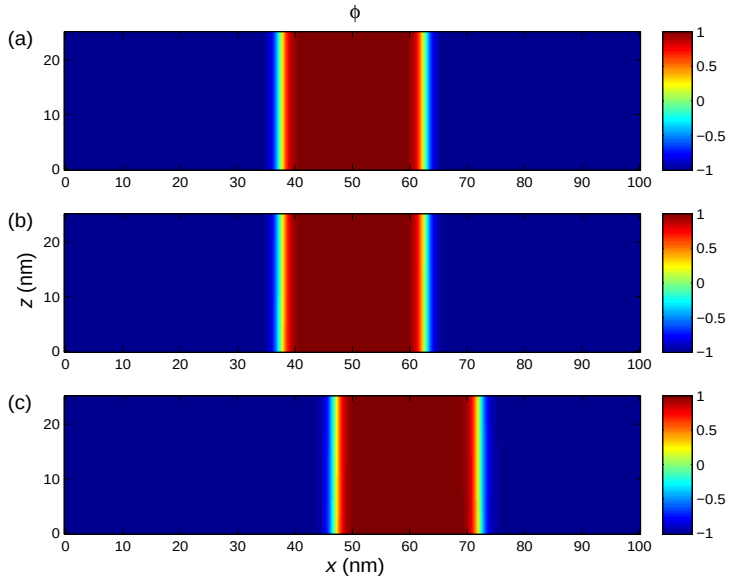

Figure 8: The order parameter fields for case (1) at (a) $t=0$, (b) $t=400$, and (c) $t=14338$.

$v_x(z)$ profiles at the left boundary become almost parabolic, as seen from Fig. 6. Compared to the plug-flow profile, the parabolic profile has the velocity variation less confined near the solid boundaries and hence acquires a lower viscous dissipation. That is,

charge transport makes the operating state less dissipative. This explains the faster flow accompanying the parabolic profile.

For comparison, we also plot the velocity fields at $t=400$ and $t=14338$ in Fig. 7. At $t=400$ in the initial stage, the $v_x(z)$ profiles far from the fluid-fluid interfaces are of plug-flow type seen in single-phase EOF. At the fluid-fluid interfaces, $v_x(z)$ shows negligible variation. Between these two distinct behaviors, there is a transition region measuring ~ 10nm in the x direction, with slip at solid surface. At $t=14338$, the $v_x(z)$ profiles far from the fluid-fluid interfaces become parabolic due to charge redistribution, as already seen in Fig. 6. The order parameter fields at three time instants are plotted in Fig. 8, which shows the movement of fluid-fluid interfaces. The interfaces are approximately flat because the capillary number $\eta U_{eo}/\gamma \sim 4\times 10^{-4}$ is very small.

4.3.2 $\theta_s=60^\circ$ and 120°

We now turn to $\theta_s=60^\circ$ and 120°. Here θ_s is measured in the side of the nonconductive fluid 2. The other parameters are $H=25$nm, $W=100$nm, $W_0=25$nm, and $E_0=10^6$V/m. In Fig. 9, we plot the fluid velocity at the center of the left boundary of the channel as a function of time for three different values of θ_s. It is observed that larger velocity is reached with smaller contact angle and this becomes more obvious as charge redistribution goes on. Physically, a smaller contact angle makes the charge less concentrated in the tiny region close to the contact line, and consequently, the MCL involves less viscous dissipation. This leads to a larger fluid flux under the same driving field. The charge density fields for $\theta_s=60^\circ$ and $\theta_s=120^\circ$ will be shown below.

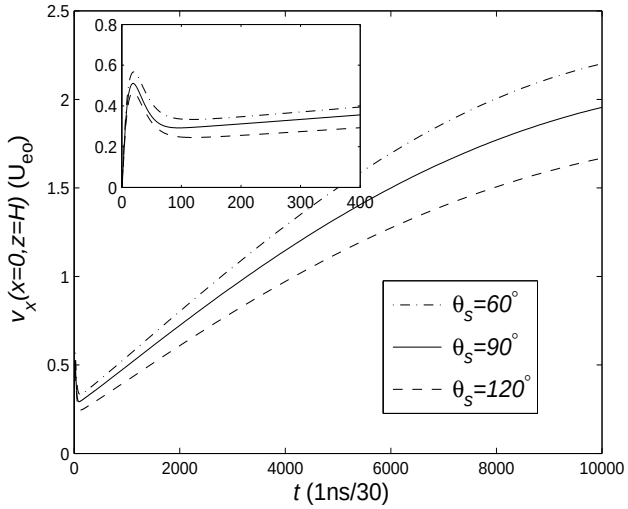

Figure 9: v_x at $(x=0,z=H)$ (the center of the left boundary of the channel) plotted as a function of time for three different static contact angles. The other parameters are $H=25$nm, $W=100$nm, $W_0=25$nm, and $E_0=10^6$V/m. The inset is an enlarged view for the initial stage from $t=0$ to 400.

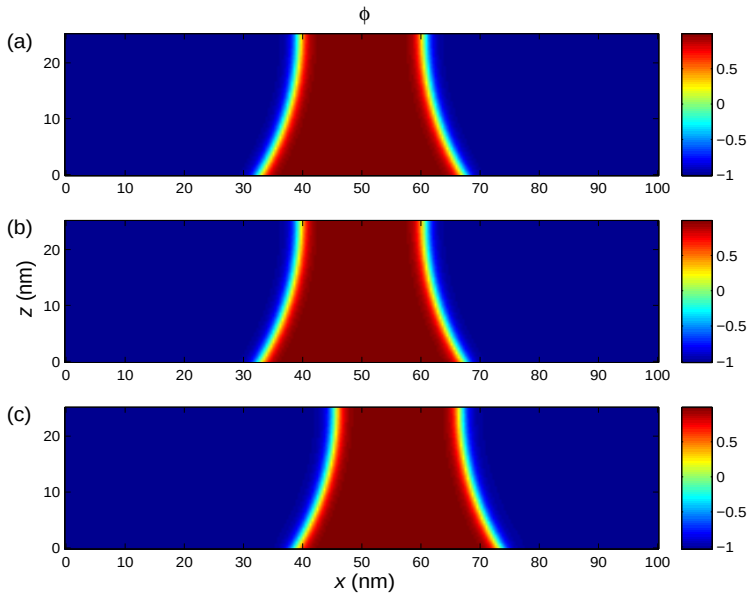

Figure 10: The order parameter fields for $\theta_s = 60^\circ$ at (a) $t = 0$, (b) $t = 400$, and (c) $t = 10000$. The two interfaces are approximately symmetric to each other even in the presence of flow because the capillary number $\eta U_{eo}/\gamma \sim 4\times 10^{-4}$ is very small.

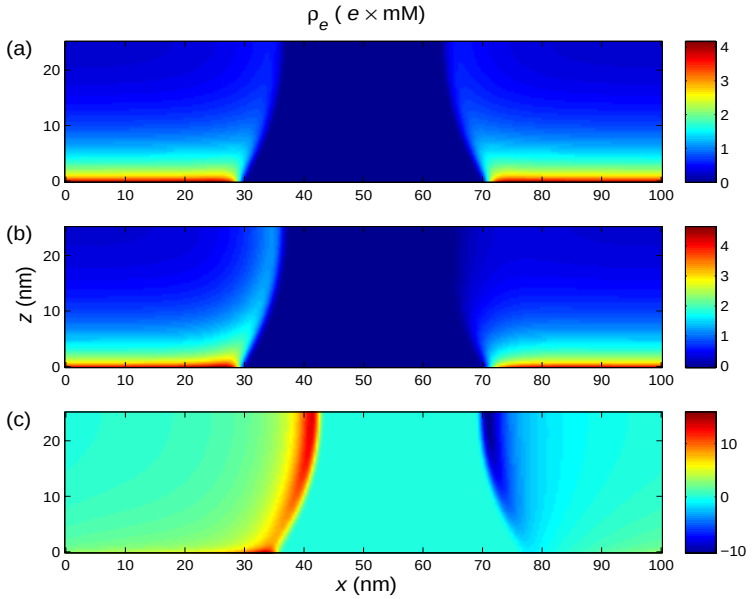

Figure 11: The net charge density fields for $\theta_s = 60^\circ$ at (a) $t = 0$, (b) $t = 400$, and (c) $t = 10000$. In (a) and (b), the charge is concentrated in the EDL next to the solid surface. Due to the slow transport in the flow, the charge gradually accumulates next to the fluid-fluid interfaces, as shown in (c).

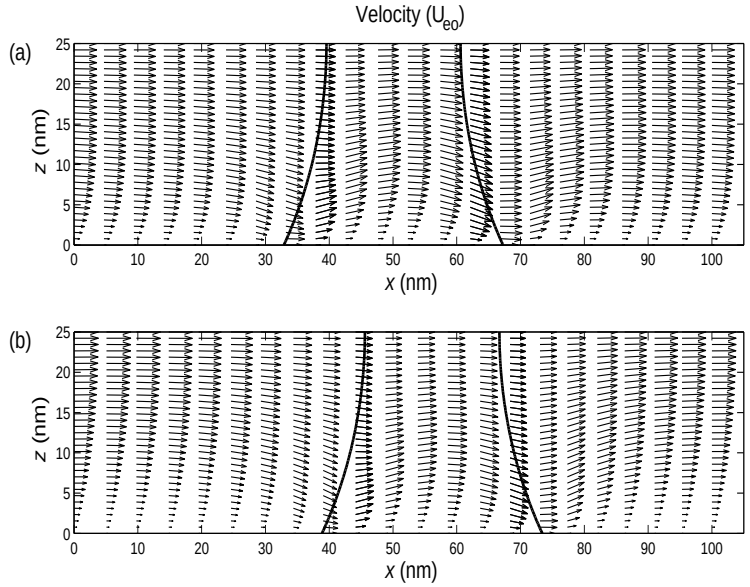

Figure 12: The velocity fields for $\theta_s = 60^\circ$ at (a) $t = 400$ and (b) $t = 10000$. The thick solid lines represent the fluid-fluid interfaces determined by $\phi = 0$. Far away from the fluid-fluid interfaces, the flow shows plug-flow profile in (a) but parabolic profile in (b), due to distinct charge distributions.

The order parameter fields at three time instants are plotted for $\theta_s = 60^\circ$ in Fig. 10, which shows the movement of fluid-fluid interfaces. The two interfaces are approximately symmetric to each other even in the presence of flow because the capillary number $\eta U_{eo}/\gamma \sim 4\times 10^{-4}$ is very small. The charge transport is illustrated in Fig. 11, which shows the charge density fields at three time instants for $\theta_s = 60^\circ$. Similar to what is observed for $\theta_s = 90^\circ$ in Fig. 5, the charge is initially concentrated in the EDL next to the solid walls, and due to the slow transport in the flow, the charge gradually accumulates next to the fluid-fluid interfaces, with positive charge on the left of the left interface and negative charge on the right of the right interface. A comparison between Fig. 5(c) and Fig. 11(c) shows that a smaller contact angle makes the charge less concentrated close to the contact line. This leads to a lower viscous dissipation and hence a larger fluid flux.

The velocity fields at $t = 400$ and $t = 10000$ are plotted for $\theta_s = 60^\circ$ in Fig. 12. Similar to what is observed for $\theta_s = 90^\circ$ in Fig. 7, far away from the fluid-fluid interfaces, the flow shows plug-flow profile in the initial stage but parabolic profile in the late stage, due to distinct charge distributions. The slip region in the vicinity of the MCL is also observed.

The order parameter fields, net charge density fields, and velocity fields for $\theta_s = 120^\circ$ are given in Fig. 13, Fig. 14, and Fig. 15, respectively. They show essentially the same salient features as those for $\theta_s = 60^\circ$. As already mentioned, it is noted that compared to Fig. 5(c) and Fig. 11(c), Fig. 14(c) shows the most concentrated charge distribution close to the contact line. This leads to the highest viscous dissipation and hence the smallest fluid flux as seen in Fig. 9.

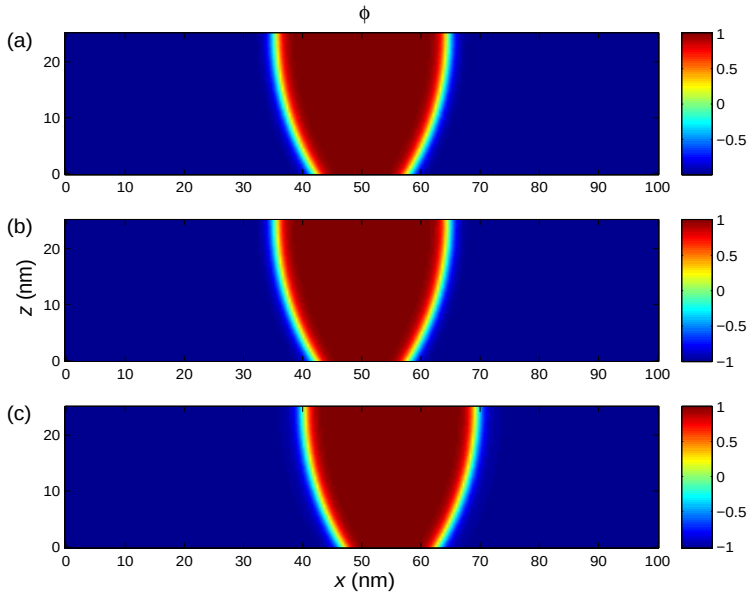

Figure 13: The order parameter fields for $\theta_s = 120^\circ$ at (a) $t = 0$, (b) $t = 400$, and (c) $t = 10000$. The two interfaces are approximately symmetric to each other even in the presence of flow because the capillary number $\eta U_{eo}/\gamma \sim 4 \times 10^{-4}$ is very small.

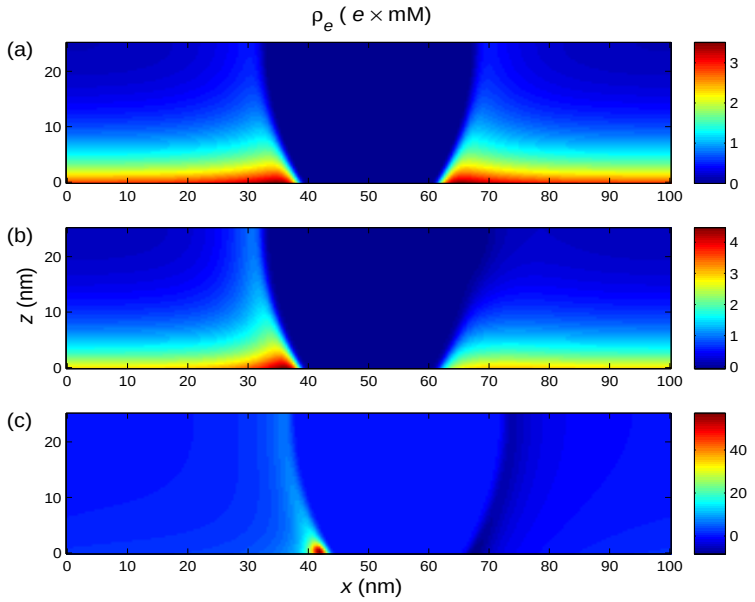

Figure 14: The net charge density fields for $\theta_s = 120^\circ$ at (a) $t = 0$, (b) $t = 400$, and (c) $t = 10000$. In (a) and (b), the charge is concentrated in the EDL next to the solid surface. Due to the slow transport in the flow, the charge gradually accumulates next to the fluid-fluid interfaces, as shown in (c).

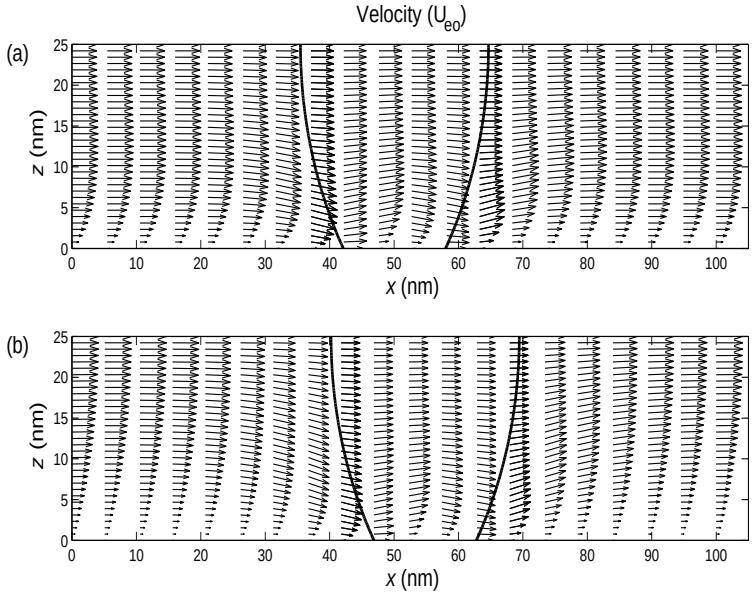

Figure 15: The velocity fields for $\theta_s = 120^\circ$ at (a) $t = 400$ and (b) $t = 10000$. The thick solid lines represent the fluid-fluid interfaces determined by $\phi = 0$. Far away from the fluid-fluid interfaces, the flow shows plug-flow profile in (a) but parabolic profile in (b), due to distinct charge distributions.

5 Concluding remarks

In this paper, we have derived a continuum hydrodynamic model for two-phase immiscible EOF at solid surfaces through a variational approach based on the Onsager principle of minimum energy dissipation [21]. This model couples the incompressible NS equation for momentum transport, the NP equation for ion transport, the CH phase-field equation for interface motion, and the Poisson equation for electric potential. In our variational approach, the boundary conditions at solid surfaces, including the GNBC for slip, are derived as the constitutive equations at fluid-solid interfaces. Numerical results in 2D channels, which involve overlapped EDL fields, have been obtained to demonstrate the validity and applicability of the model, and a few salient features of two-phase immiscible EOF at solid surfaces, including the Smoluchowski slip in the EDL and the wall slip in the vicinity of MCL.

Compared to the model presented in [28] for electrowetting, our model uses two concentrations for cations and anions to describe the EDL, with the surface charge density explicitly taken into account. The structure of EDL and the Smoluchowski slip therein have been demonstrated in Section 4.2. Our model also introduces a phase-field barrier that prevents ions from penetrating through the fluid-fluid interface into the nonconductive fluid. Numerical results in Section 4.3 have shown the blocking effect of this barrier on ion transport. The problem encountered in long-time computations in [28] is therefore avoided. Finally, the GNBC is explicitly employed in our numerical implementation,

while in [28] the numerical examples are presented with the no-slip condition.

Motivated by the results presented here, we plan to apply our model to investigate the electrowetting dynamics with a focus on the boundary slip and the charge transport in electrolyte droplets. We also plan to extend our model to incorporate a diffuse charge layer bound at the fluid-fluid interface [31, 32]. Finally, the finite size (excluded volume) effects in ionic solutions [62] are worth exploration as well. It is expected that the steric effects due to the finite size of ions will lower the high concentration near the MCL, as shown in Fig. 14, due to a balance between the electric driving force and the hard sphere repulsion.

Acknowledgments

We would like to thank Professor Chun Liu for helpful discussions and comments on the early stages of this work. This publication is based on work partially supported by Award No. SA-C0040/UK-C0016, made by King Abdullah University of Science and Technology (KAUST), and Hong Kong RGC grant No. 603510. Sihong Shao is also supported by the National Natural Science Foundation of China (No. 11101011), and the State Key Laboratory of ASIC & System (Fudan University) under the open project fund No. 10KF015.

References

[1] H. A. Stone, A. D. Stroock, and A. Ajdari. Engineering flows in small devices: Microfluidics toward a Lab-on-a-Chip. Annu. Rev. Fluid Mech., 36:381–411, 2004.
[2] G. Karniadakis, A. Beskok, and N. Aluru. Microflows and Nanoflows: Fundamentals and Simulation. Springer, New York, 2005.
[3] D. Erickson and D. Q. Li. Microscale flow and transport simulation for electrokinetic and lab-on-chip applications. In R. Bashir and S. Wereley, editors, Biomems and Biomedical Nanotechnology, Volume IV: Biomolecular Sensing, Processing and Analysis, pages 277–300. Springer, New York, 2006.
[4] G. Goranović. Electrohydrodynamic aspects of two-fluid microfluidic systems: theory and simulation. PhD thesis, Technical University of Denmark, 2003.
[5] S. Ghosal. Electrokinetic flow and dispersion in capillary electrophoresis. Annu. Rev. Fluid Mech., 38:309–338, 2006.
[6] C. Neto, D. R. Evans, E. Bonaccurso, H. J. Butt, and V. S. J. Craig. Boundary slip in Newtonian liquids: A review of experimental studies. Rep. Prog. Phys., 68:2859–2897, 2005.
[7] A. Ajdari and L. Bocquet. Giant amplification of interfacially driven transport by hydrodynamic slip: Diffusio-osmosis and beyond. Phys. Rev. Lett., 96:186102, 2006.
[8] J. C. T. Eijkel. Liquid slip in micro- and nanofluidics: Recent research and its possible implications. Lab Chip, 7:299–301, 2007.
[9] E. Lauga, M. P. Brenner, and H. A. Stone. Microfluidics: The no-slip boundary condition. In C. Tropea, A. Yarin, and J. F. Foss, editors, Handbook of Experimental Fluid Mechanics, pages 1219–1240. Springer, Berlin, 2007.
[10] H. Song, D. L. Chen, and R. F. Ismagilov. Reactions in droplets in microfluidic channels. Angew. Chem. Int. Ed., 45:7336–7356, 2006.

[11] A. Huebner, S. Sharma, M. Srisa-Art, F. Hollfelder, J. B. Edel, and A. J. deMello. Microdroplets: A sea of applications? Lab Chip, 8:1244–1254, 2008.
[12] O. Kuksenok, D. Jasnow, J. Yeomans, and A. C. Balazs. Periodic droplet formation in chemically patterned microchannels. Phys. Rev. Lett., 91:108303, 2003.
[13] S. L. Anna, N. Bontoux, and H. A. Stone. Formation of dispersions using "flow focusing" in microchannels. Appl. Phys. Lett., 82:364–366, 2003.
[14] H. K. Moffatt. Viscous and resistive eddies near a sharp corner. J. Fluid Mech., 18:1–18, 1964.
[15] C. Huh and L. E. Scriven. Hydrodynamic model of steady movement of a solid/liquid/fluid contact line. J. Colloid Interface Sci., 35:85–101, 1971.
[16] E. B. Dussan V. On the spreading of liquids on solid surfaces: Static and dynamic contact lines. Annu. Rev. Fluid Mech., 11:371–400, 1979.
[17] P. G. de Gennes. Wetting: Statics and dynamics. Rev. Mod. Phys., 57:827–863, 1985.
[18] D. Bonn, J. Eggers, J. Indekeu, J. Meunier, and E. Rolley. Wetting and spreading. Rev. Mod. Phys., 81:739–805, 2009.
[19] T. Z. Qian, X. P. Wang, and P. Sheng. Molecular scale contact line hydrodynamics of immiscible flows. Phys. Rev. E, 68:016306, 2003.
[20] T. Z. Qian, X. P. Wang, and P. Sheng. Molecular hydrodynamics of the moving contact line in two-phase immiscible flows. Commun. Comput. Phys., 1:1–52, 2006.
[21] T. Z. Qian, X. P. Wang, and P. Sheng. A variational approach to moving contact line hydrodynamics. J. Fluid Mech., 564:333–360, 2006.
[22] L. Onsager. Reciprocal relations in irreversible processes. I. Phys. Rev., 37: 405–426, 1931.
[23] L. Onsager. Reciprocal relations in irreversible processes. II. Phys. Rev., 38: 2265–2279, 1931.
[24] W. Ren and W. E. Boundary conditions for moving contact line problem. Phys. Fluids, 19: 022101, 2007.
[25] M.-C. Audry, A. Piednoir, P. Joseph, and E. Charlaix. Amplification of electro-osmotic flows by wall slippage: Direct measurements on OTS-surfaces. Faraday Discuss., 146:113-124, 2010.
[26] Y. Ren and D. Stein. Slip-enhanced electrokinetic energy conversion in nanofluidic channels. Nanotechnology, 19:195707, 2008.
[27] F. Mugele and J. C. Baret. Electrowetting: From basics to applications. J. Phys.: Condens. Matter, 17:R705–R774, 2005.
[28] C. Eck, M. Fontelos, G. Grün, F. Klingbeil, and O. Vantzos. On a phase-field model for electrowetting. Interfaces Free Boundaries, 11:259–290, 2009.
[29] D. A. Saville. Electrohydrodynamics: The Taylor-Melcher leaky dielectric model. Annu. Rev. Fluid Mech., 29:27–64, 1997.
[30] G. Tomar, D. Gerlach, G. Biswas, N. Alleborn, A. Sharma, F. Durst, S. W. J. Welch, and A. Delgado. Two-phase electrohydrodynamic simulations using a volume-of-fluid approach. J. Comput. Phys., 227:1267–1285, 2007.
[31] S. Mählmann and D. T. Papageorgiou. Numerical study of electric field effects on the deformation of two-dimensional liquid drops in simple shear flow at arbitrary Reynolds number. J. Fluid Mech., 626:367–393, 2009.
[32] Y. D. Gao, T. N. Wong, C. Yang, and K. T. Ooi. Two-fluid electroosmotic flow in microchannels. J. Colloid Interface Sci., 284:306–314, 2005.
[33] D. C. Grahame. The electrical double layer and the theory of electrocapillarity. Chem. Rev., 41:441–501, 1947.
[34] C. Yang and D. Q. Li. Electrokinetic effects on pressure-driven liquid flows in rectangular microchannels. J. Colloid Interface Sci., 194:95–107, 1997.

[35] R. J. Yang, L. M. Fu, and Y. C. Lin. Electroosmotic flow in microchannels. J. Colloid Interface Sci., 239:98–105, 2001.
[36] D. Stein, M. Kruithof, and C. Dekker. Surface-charge-governed ion transport in nanofluidic channels. Phys. Rev. Lett., 93:035901, 2004.
[37] F. H. J. van der Heyden, D. Stein, and C. Dekker. Streaming currents in a single nanofluidic channel. Phys. Rev. Lett., 95:116104, 2005.
[38] W. L. Qu and D. Q. Li. A model for overlapped EDL fields. J. Colloid Interface Sci., 224:397–407, 2000.
[39] H. S. Kwak and E. F. Hasselbrink Jr. Timescales for relaxation to Boltzmann equilibrium in nanopores. J. Colloid Interface Sci., 284:753–758, 2005.
[40] H. M. Park, J. S. Lee, and T. W. Kim. Comparison of the Nernst-Planck model and the Poisson-Boltzmann model for electroosmotic flows in microchannels. J. Colloid Interface Sci., 315:731–739, 2007.
[41] L. M. Fu, J. Y. Lin, and R. J. Yang. Analysis of electroosmotic flow with step change in zeta potential. J. Colloid Interface Sci., 258:266–275, 2003.
[42] D. Hlushkou, D. Kandhai, and U. Tallarek. Coupled lattice-Boltzmann and finite-difference simulation of electroosmosis in microfluidic channels. Int. J. Numer. Mech. Fluids, 46:507–532, 2004.
[43] H. Daiguji, P. D. Yang, and A. Majumdar. Ion transport in nanofluidic channels. Nano Lett., 4:137–142, 2004.
[44] H. Daiguji, P. D. Yang, A. J. Szeri, and A. Majumdar. Electrochemomechanical energy conversion in nanofluidic channels. Nano Lett., 4:2315–2321, 2004.
[45] H. Daiguji, T. Adachi, and N. Tatsumi. Ion transport through a T-intersection of nanofluidic channels. Phys. Rev. E, 78:026301, 2008.
[46] K. D. Huang and R. J. Yang. Electrokinetic behaviour of overlapped electric double layers in nanofluidic channels. Nanotechnology, 18:115701, 2007.
[47] A. Onuki. Ginzburg-Landau theory of solvation in polar fluids: Ion distribution around an interface. Phys. Rev. E, 73:021506, 2006.
[48] S. Kang and Y. K. Suh. Numerical analysis on electroosmotic flows in a microchannel with rectangle-waved surface roughness using the Poisson-Nernst-Planck model. Microfluid. Nanofluid., 6:461–477, 2009.
[49] S. Kang and Y. K. Suh. Electroosmotic flows in an electric double layer overlapped channel with rectangle-waved surface roughness. Microfluid. Nanofluid., 7:337–352, 2009.
[50] S. Pennathur, J. C. T. Eijkel, and A. van den Berg. Energy conversion in microsystems: Is there a role for micro/nanofluidics? Lab Chip, 7:1234–1237, 2007.
[51] L. Joly, C. Ybert, E. Trizac, and L. Bocquet. Hydrodynamics within the electric double layer on slipping surfaces. Phys. Rev. Lett., 93:257805, 2004.
[52] J. F. Dufrêche, V. Marry, N. Malíková, and P. Turq. Molecular hydrodynamics for electroosmosis in clays: From Kubo to Smoluchowski. J. Mol. Liq., 118:145–153, 2005.
[53] L. Joly, C. Ybert, E. Trizac, and L. Bocquet. Liquid friction on charged surfaces: From hydrodynamic slippage to electrokinetics. J. Chem. Phys., 125:204716, 2006.
[54] D. M. Anderson, G. B. McFadden, and A. A. Wheeler. Diffuse-interface methods in fluid mechanics. Annu. Rev. Fluid Mech., 30:139–165, 1998.
[55] D. Jacqmin. Contact-line dynamics of a diffuse fluid interface. J. Fluid Mech., 402:57-88, 2000.
[56] P. Yue, C. Zhou, and J. J. Feng. Sharp-interface limit of the Cahn-Hilliard model for moving contact lines. J. Fluid Mech., 645:279-294, 2010.

[57] R. Ryham, C. Liu, and L. Zikatanov. Mathematical models for the deformation of electrolyte droplets. Discrete Cont. Dyn. Syst.-B, 8:649–661, 2007.
[58] H. Johnston and J. G. Liu. Finite difference schemes for incompressible flow based on local pressure boundary conditions. J. Comput. Phys., 180:120–154, 2002.
[59] D. J. Eyre. An unconditionally stable one-step scheme for gradient systems. preprint, 1997.
[60] S. Selberherr. Analysis and Simulation of Semiconductor Devices. Springer-Verlag, Wien-New York, 1984.
[61] H. C. Kim and D. J. Burgess. Prediction of interfacial tension between oil mixtures and water. J. Colloid Interface Sci., 241:509–513, 2001.
[62] Y. Hyon, B. Eisenberg and C. Liu. A mathematical model for the hard sphere repulsion in ionic solutions. Commun. Math. Sci., 9(2):459–475, 2011.